

AperTO - Archivio Istituzionale Open Access dell'Università di Torino

Theoretical and Experimental Characterization of Pyrazolato-Based Ni(II) Metal Organic Frameworks

This is the author's manuscript

Original Citation:

Availability:

This version is available <http://hdl.handle.net/2318/117528> since 2016-08-04T15:15:48Z

Published version:

DOI:10.1039/C2JM34079H

Terms of use:

Open Access

Anyone can freely access the full text of works made available as "Open Access". Works made available under a Creative Commons license can be used according to the terms and conditions of said license. Use of all other works requires consent of the right holder (author or publisher) if not exempted from copyright protection by the applicable law.

(Article begins on next page)



UNIVERSITÀ DEGLI STUDI DI TORINO

This is an author version of the contribution published on:

E. Albanese, B. Civalleri, M. Ferrabone, F. Bonino, S. Galli, A. Maspero,
C. Pettinari
Theoretical and Experimental Characterization of Pyrazolato-Based Ni(II)
Metal Organic Frameworks.
Journal of Materials Chemistry, 22, 22592-22602, 2012, DOI:
10.1039/C2JM34079H.

The definitive version is available at:

<http://pubs.rsc.org>

Theoretical and Experimental Characterization of Pyrazolato-Based Ni(II) Metal Organic Frameworks[†]

Elisa Albanese,^a Bartolomeo Civalleri,^{*a} Matteo Ferrabone,^a Francesca Bonino,^a Simona Galli,^b Angelo Maspero,^b Claudio Pettinari^c

Received Xth XXXXXXXXXXXX 20XX, Accepted Xth XXXXXXXXXXXX 20XX

First published on the web Xth XXXXXXXXXXXX 200X

DOI: 10.1039/b000000x

The structural, electronic, dielectric and vibrational features of two metal-organic frameworks with bispyrazolate ligands are investigated by combining ab-initio periodic calculations and experimental techniques. UV-Vis spectroscopy has been used to study the electronic structure, while FTIR spectroscopy to obtain information about the vibrational features of the samples and their adsorptive properties. The examined MOFs contain square-planar Ni(II) nodes bridged either by the 4,4'-bispyrazolato (bpz) or by the 1,4-bis(4-pyrazolato)benzene (bpb) spacers. As expected, they are diamagnetic solids, with Ni(II) in low spin state. This has been confirmed through computed results, other magnetic phases being predicted remarkably less stable. Both materials possess a band gap of ~ 3.4 eV and show interesting dielectric properties due to the microporous structure and the low dielectric constant. Although Ni(II) is coordinatively unsaturated, it does not show any specific interaction with the probe molecules tested, as evidenced by FTIR measurements. This unexpected behavior is explained on the basis of computed results. The high stability of the low spin state of Ni(II) in square-planar coordination and a reduced accessibility of the metal sites due to steric effects are considered the reasons for the absence of preferential interactions between the metal centers and the probe molecules adopted.

1 Introduction

In the last years Metal Organic Frameworks (MOFs), a new class of crystalline porous materials, have attracted a lot of interest because of their great compositional variety and their advanced technological applications.¹⁻⁵ Indeed, these materials can be designed starting from building units such as metallic ions or oxo-metallic clusters (node) linked by poly-dentate organic ligands (spacer) to form a three-dimensional framework with stable and well-defined cavities.¹ They are mainly known for oxygen-donor ligands, mostly carboxylates, coupled to many different metal ions, including transition metals, 4f and even alkaline earth elements.¹

Recently, polyazolato-based ligands containing tetrazolato, triazolato, imidazolato or pyrazolato moieties have been used as a mean to build porous MOFs possessing a higher thermal and chemical stability than the carboxylato-based counterparts. In these materials, the strength of the M-N bond can be considered closely related to the pKa value of the N-H bond of the parent azolyl ligand. In line with this consideration, cornerstone results, in terms of thermal stability, have been obtained by Yaghi and coworkers with imidazolato-containing struts⁶ and by the groups of Long and Kitagawa with pyrazolato-based spacers.⁷⁻⁹ To further explore the potentiality of this strategy, Masciocchi et al.¹⁰ devised a cheap and highly efficient synthesis for novel bispyrazole ligands and investigated their coordination chemistry toward Ni(II)^{11,12} and Zn(II)¹¹, isolating and characterizing porous materials possessing high thermal robustness, with potential interest for their adsorptive properties.

In this work, our aim is to investigate the structural, electronic and vibrational features of two pyrazolato-based Ni(II) MOFs by means of a combined use of ab-initio computational modelling and experimental techniques; in particular, UV-Vis spectroscopy has been used to study their electronic structure, while Fourier transform infrared spectroscopy (FTIR) has been adopted to obtain information about their vibrational features and adsorptive properties. This approach has recently been applied, by some of us, to the study of several

[†] Electronic Supplementary Information (ESI) available: [(i) Relative stability of magnetic phases (Table S1); (ii) FTIR spectra of samples activation for Ni-bpz and Ni-bpb (Figures S1-S2); (iii) FTIR spectra of the adsorption of CO and CO₂ in Ni-bpb (Figures S3-S4); (iv) Simulated and experimental FTIR spectra in the spectral region above 2900 cm⁻¹ for Ni-bpz and Ni-bpb (Figure S5); (v) Graphical results of the Rietveld refinement carried out on Ni-bpz (Figure S6); (vi) CRYSTAL input files with the optimized geometries of Ni-bpz and Ni-bpb; (vii) Calculated IR and Raman vibrational frequencies for Ni-bpz and Ni-bpb (Tables S2-S5)]. See DOI: 10.1039/b000000x/

^a Dipartimento di Chimica and Centro di eccellenza NIS, Via P. Giuria 7, 10129 Università di Torino, Torino, Italy; E-mail: bartolomeo.civalleri@unito.it

^b Dipartimento di Scienza e Alta Tecnologia, Università dell'Insubria, Via Valleggio 11, I-22100 Como, Italy

^c Dipartimento di Scienze del Farmaco e dei Prodotti della Salute, Università di Camerino, Via S. Agostino 1, I-62032 Camerino (MC), Italy

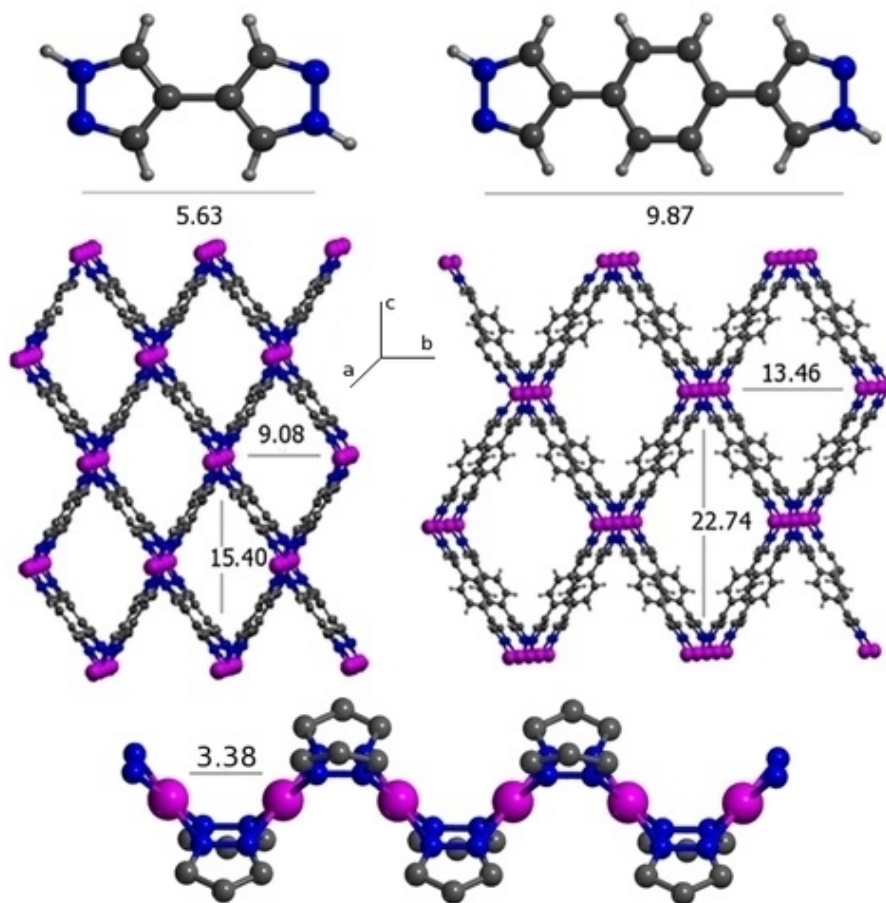


Fig. 1 H₂bpz and H₂bpb ligands (top), the experimental structure of the corresponding Ni-bpz and Ni-bpb metal organic frameworks (middle) and the linear chain of square-planar Ni(II) atoms (bottom). Distances (in Å): N···N (top), Ni···Ni (middle and bottom). Ni in magenta, N in blue, C in gray and H in white.

MOFs, such as UiO-66¹³, UiO-67¹⁴ and CPO-27-M (M=Mg, Ni).^{15,16}

The two MOFs under investigation, hereafter denoted Ni-bpz and Ni-bpb, possess the same structural topology of the MIL-53 family¹⁷, built up by coupling the 4,4'-bispyrazolato (bpz) and 1,4-bis(4-pyrazolato)benzene (bpb) ligands to square planar, coordinatively unsaturated Ni(II) ions (see Figure 1). As exposed metal sites, in MOFs, are known to be primary interaction sites with gaseous hydrogen¹⁸, molecular hydrogen has then been used as a probe to investigate the adsorption capability of Ni-bpb. We anticipate that, surprisingly, the coordinatively unsaturated Ni(II) ions do not show any specific interaction with dihydrogen. Theoretical results will be used to shed some light on this apparently unexpected behavior.

2 Experimental and computational details

2.1 Synthesis

Both MOFs were synthesized by following the procedures already reported in the literature^{11,19}. Before any spectroscopic investigation, the purity and crystallinity of the prepared specimens were determined by means of XRPD

2.2 X-ray powder diffraction data acquisition

The as-synthesized materials host, in the channels, clathrated solvent molecules. To grant a more consistent comparison between the XRPD-derived and the ab-initio calculated structural details, the crystal structures of the desolvated materials, conserving the same structural topology of the parent specimens, were taken into consideration. As observed by FT-IR spectroscopy (Figure S2), as-synthesized Ni-bpb can be easily evacuated by thermal treatment under high vacuum. More-

over, as already demonstrated¹¹, evacuated Ni-bpb does not show propensity to adsorb water from moisture. In the case of Ni-bpz, complete evacuation appears to be hardly attainable (Figure S1), even after prolonged thermal treatment under high vacuum. Moreover, when left at room temperature, activated Ni-bpz shows some tendency to adsorb moisture, as witnessed by the change, in time, of its unit cell metrics¹¹. Thus, to grant a trade-off between low solvent content and appreciable degree of crystallinity, the structural details of Ni-bpz were determined by means of an XRPD structural analysis carried out on laboratory data acquired at 130 °C, by adopting the following procedure. A powdered, microcrystalline sample of the material was ground in an agate mortar; then, it was deposited in the hollow of an aluminum sample holder equipped with a zero-background plate. The diffraction data were collected at 130 °C by coupling a custom-made sample heater (assembled by Officina Elettrotecnica di Tenno, Ponte Arche, Italy) to a Bruker AXS D8 Advance diffractometer, equipped with Ni-filtered Cu-K α radiation ($\lambda = 1.5418 \text{ \AA}$) and with a Lynxeye linear position-sensitive detector, and mounting the following optics: primary beam Soller slits (2.3°), fixed divergence slit (0.5°), receiving slit (8 mm). The generator was set at 40 kV and 40 mA. An overnight scan was performed in the 5-105° 2θ range, with 0.02° steps. The refinement of the crystal structure was performed by the Rietveld method as implemented in TOPAS (TOPAS-R, version 3.0, Bruker AXS, 2005, Karlsruhe, Germany). As starting model, that derived from the room temperature structure determination was adopted¹⁹, which described the crystallographically independent portion of the ligand with a rigid body, * imposing idealized bond distances and angles (C-C, C-N, N-N of the heterocyclic ring 1.36 Å; C-C 1.50 Å; C-H, N-H = 0.95 Å; heterocyclic ring internal bond angles 108°). Being relevant for the following discussion, it is worth noting here that a rigid body model was adopted also for Ni-bpb (C-C of the phenylene ring 1.39 Å; phenylene ring internal bond angles 120°). The background was modeled by a Chebyshev polynomial function. The thermal effect was simulated by using a single isotropic parameter for the metal ion, augmented by 2.0 Å² for lighter atoms. Rietveld refinement plot for Ni-bpb is available in ref.¹¹, while that for the high temperature phase of Ni-bpz is supplied as Figure S6 in the ESI. Crystal data for Ni-bpz: C₆H₄N₄Ni, FW = 190.82 g/mol, orthorhombic, *Imma*, $a = 14.939(4) \text{ \AA}$, $b = 6.839(1) \text{ \AA}$, $c = 9.588(3) \text{ \AA}$, $V = 979.5(4) \text{ \AA}^3$; $Z = 4$; $\rho_{calc} =$

1.29 g cm⁻³; $F(000) = 384$; $\mu(\text{CuK}) = 24.5 \text{ cm}^{-1}$. R_p , R_{wp} , and R_{Bragg} are 0.023, 0.035 and 0.012, respectively, for 21 parameters.

2.3 Spectroscopic measurements

FTIR spectroscopic measurements were performed using a homemade cryogenic cell²⁰⁻²² that allows to perform (i) *in situ* high-temperature activation of the sample under a high vacuum and (ii) variable temperature infrared (VTIR)²²⁻²⁹ spectroscopy of the adsorbed species while simultaneously measuring temperature and equilibrium pressure. For FTIR spectroscopy, a thin self-supported wafer of the samples was prepared and activated under high vacuum (residual pressure < 10⁻⁴ mbar) at 453 K for 2 h. FTIR spectra were collected, at 2 cm⁻¹ resolution, on a Bruker IFS 66 FTIR spectrometer equipped with a MCT and a DTGS detector.

DRS-UV-vis-NIR measurements were performed on a Varian Cary 5000 spectrometer equipped with a reflectance sphere on powdered samples. In order to avoid saturation and to consider the relative intensity of the bands, the samples were diluted with teflon.

2.4 Computational details

The theoretical investigation of Ni-bpb and Ni-bpz was carried out with periodic density functional theory (DFT) calculations employing the hybrid B3LYP^{30,31} functional as implemented in the CRYSTAL program^{32,33}. This computational approach has been successfully applied to study other MOFs^{13-15,34-36}.

Crystalline orbitals are represented as linear combinations of Bloch functions (BF), and are evaluated over a regular three-dimensions mesh of points in reciprocal space. Each BF is built from local atomic orbitals (AO), which are contractions (linear combinations with constant coefficients) of Gaussian-type-functions (GTF) which in turn are the product of a Gaussian times a real solid spherical harmonic function. An all electron basis set has been used for Ni, C, N and H; namely modified triple- ζ valence plus polarization (TZVP) for Ni^{16,37}, and 6-311G(d,p) for H, C and N.

For the numerical integration of the exchange-correlation term, 75 radial points and 974 angular points in a Lebedev scheme in the region of chemical interest were adopted. The Pack-Monkhorst/Gilat shrinking factors for the reciprocal space were set to 3 and 6, corresponding to 10 and 68 real and reciprocal space points at which the Hamiltonian matrix was diagonalized. The accuracy of the integral calculations was increased by setting the tolerances to 7, 7, 7 and 20. The self-consistent field (SCF) iterative procedure was converged to a tolerance in total energy of $\Delta E = 1 \cdot 10^{-7}$ a.u..

To accelerate convergence in the self-consistent calculations a modified Broyden's scheme³⁸ following the method proposed

* The use of rigid bodies to describe (part of) the asymmetric unit is a common procedure, adopted already in the 1990s, for structure determinations from powder diffraction data. Facilitated by the evidence that, in organic moieties, bond distances and angles typically possess well established values, the adoption of rigid bodies aims, *inter alia*, to decrease the number of refined parameters, thus improving the rather low data-to-parameters ratio typical of powder diffraction acquisitions, which may severely impede convergence to a chemically and physically sensible model, also during the final stages of a Rietveld refinement.

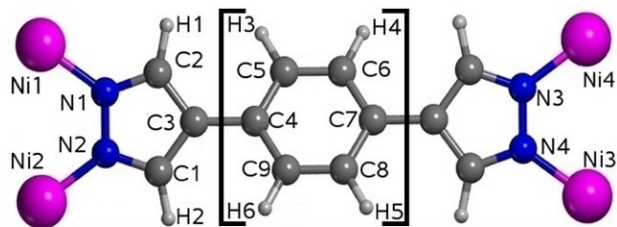


Fig. 2 Labelling of the atoms as used in Table 1 and in the text for Ni-bpz (without the aromatic ring in the square brackets) and Ni-bpb.

by Johnson³⁹ was adopted; the method was applied after ten SCF iterations, with 50% of Fock/KS matrices mixing and with the Johnson parameter set to 0.05. The above computational parameters ensured a full numerical convergence on all the computed properties described in this work.

Vibrational frequencies at the Γ point and their IR intensities were calculated on the optimized geometry by means of a mass-weighted Hessian matrix, obtained by numerical differentiation of the analytical first derivatives.^{40,41}

Unit cell polarizability and the dielectric tensor at the static limit (i.e. $\omega = 0$) were computed by using the CPKS scheme for periodic systems recently implemented in the CRYSTAL code.^{42–44} The convergence is checked on the stability of the diagonal elements of the polarizability. The convergence criterion adopted stops the process when these elements differ by less than 10^{-4} au in two successive cycles. From the unit cell polarizability tensor, α_{ij} , the first-order susceptibility $\chi^{(1)}$ and the dielectric tensor components ϵ_{∞} are obtained as:

$$\chi_{ij}^{(1)} = \frac{4\pi}{V} \alpha_{ij} \quad (1)$$

$$\epsilon_{\infty,ij} = \chi_{ij}^{(1)} + \delta_{ij} \quad (2)$$

where $\delta_{ij} = 1$ if $i = j$ and 0 for $i \neq j$. Refractive index at the static limit can also be computed as: $n_{ij} = \epsilon_{\infty,ij}^{1/2}$.

3 Results and Discussion

3.1 Geometry

The main structural features, as retrieved from XRPD, are hereafter recalled for the sake of comprehension. The two isomorphous materials crystallize in the orthorhombic *Imma* space group. The asymmetric unit contains one Ni(II) ion, located on a special position, and 1/4 of the ligand. Each metal center is coordinated to four nitrogen atoms of four distinct ligands in square-planar stereochemistry, thus possessing two coordinative vacancies (see Figure 1 bottom). This feature has already been found in simpler analogues, such as the nickel imidazolate⁴⁵ and pyrazolate species⁴⁶. With their pyrazolato

moieties, the ligands bridge adjacent Ni(II) ions, and generate linear and parallel chains of metal centers running along the crystallographic axis a . The chains, further connected by the bpz and bpb spacers along b and c , generate a tridimensional network featuring monodimensional channels of rhombic shape (with dimensions of 9.1×15.4 Å and 13.4×22.7 Å; see Figure 1 middle). In the desolvated materials, the channels represent about the 42% and 57% of the crystal volume, for Ni-bpz and Ni-bpb, respectively (as calculated by Platon⁴⁷). Along the chains, the bridged Ni(II) ions are kept at a distance of about 3.4 Å. Although the distance between two adjacent, coordinatively unsaturated, metal ions would be large enough to permit the adsorption of small molecules, such as CO₂, CO and H₂, unexpectedly, no evidence of interaction is observed, as will be discussed later on for H₂.

Before comparing the calculated structural features to the XRPD-derived ones, it is interesting to briefly discuss the magnetic features of the examined MOFs. As expected for Ni(II) in square planar coordination⁴⁸, the most stable magnetic phase is predicted by theoretical calculations, to have Ni(II) in the low spin state. Other phases with Ni(II) in high spin configuration were also investigated theoretically, but they resulted to be very unstable with a relative stability of more than 65 kJ per mole of Ni atoms (see ESI for details). Therefore, the theoretical results and the well-known propensity of Ni(II), in square planar coordination, to be in a low spin state strongly suggest that both MOFs are diamagnetic materials. Hereafter, all computed results refer to the diamagnetic phase.

As far as the structural features of Ni-bpz and Ni-bpb are concerned, the computed lattice parameters and the relevant structural features of both materials are gathered in Table 1 and compared with the experimental data obtained from X-ray powder diffraction. In the Ni-bpb case, the experimental structure with the *Imma* space group is not a minimum on the potential energy surface because it shows several imaginary frequencies related to the rotation of the phenyl rings. Therefore, by following the lowest imaginary vibrational modes, a lowering of the symmetry from *Imma* to *I112/b* was observed, with the phenylene rings no more constrained to be co-planar with the pyrazolato groups.[†] Interestingly, the lowering of the symmetry does not cause a significant deformation of the unit cell. Indeed, the cell can still be considered

[†] It is worth to underline that the strict planarity of the bpb ligand in the XRPD-derived model is not dictated by the adoption of a rigid body; a non-planar (hence disordered in *Imma*) ligand, with the rings free to rotate around the C-C exocyclic bonds, can be in principle admitted. Indeed, at the time of finalizing the work appeared in Ref. ¹¹, this possibility was taken into consideration. Yet, no significant difference could be appreciated between the two models: the simplest one, featuring an ordered ligand, was then privileged. As a further proof, we have evaluated the r.m.s. of the distances between the crystallographically independent atoms of the ligand in *Imma* and *I112/b*: a value of ca. 0.15 Å has been obtained, which is hardly discriminated by (either powder or single crystal) diffraction.

Table 1 Calculated and experimental geometry of diamagnetic Ni-bpz and Ni-bpb structures (volume in Å³, lattice parameters and bond distances in Å, bond angles in degrees and density in g/cm³). See Figure 2 for atomic labels

	Ni-bpz			Ni-bpb		
	Calc	Exp ^b	Δ% ^a	Calc	Exp ^{11,b}	Δ% ^a
Volume	1040.246	974.466	6.3	2293.177	2071.103	10.7
<i>a</i>	7.027	6.851	2.5	7.012	6.766	3.6
<i>b</i>	14.597	14.999	-2.8	21.728	22.735	-4.4
<i>c</i>	10.142	9.482	6.5	15.052	13.465	11.8
β	90.00	90.00		89.78	90.00	
Density	1.21	1.29		0.77	0.86	
Ni1-Ni2	3.513	3.426		3.506	3.383	
Ni1-Ni4	8.887	8.872		13.216	13.212	
Ni1-N1	1.910	1.860		1.909	1.973	
N1-N2	1.352	1.357		1.354	1.360	
N1-C2	1.344	1.358		1.342	1.360	
C3-C3'	1.457	1.460				
C3-C4				1.469	1.450	
C4-C5				1.403	1.390	
C5-C6				1.389	1.390	
Ni1-N1-C2	127.07	128.36		127.63	130.15	
Ni1-N1-N2	124.47	123.63		124.05	120.84	
C1-N2-N1	108.26	108.00		108.24	108.00	
N1-C2-C3	110.10	108.00		110.11	108.00	
C1-C2-C3	103.27	108.00		103.28	108.00	
N1-Ni1-N1'	89.21	87.41		89.25	84.62	
N1-Ni1-N2	90.79	92.59		90.75	95.38	

^a percentage deviation from experiment

^b as detailed in the Experimental Section, the ligands were modeled by adopting rigid bodies

pseudo-orthorhombic, with the values of the β angle being not so different from 90 degrees.

For both materials, sizable differences between the calculated and experimental *c* lattice constant are found. Indeed, *c* is overestimated by more than 6% for Ni-bpz and 10% for Ni-bpb, while *b* is underestimated by some 3-5% for both MOFs. Instead, the direction along which the metallic chains grow (*a*) is only slightly modified (see Table 1). According to our experience, differences in the range 3-5% are normally found when comparing the calculated unit cells with those derived from XRPD data at very low temperatures (e.g. 20 K). At least in principle, higher discrepancies are expected if, as in the present work, the calculated parameters are compared with those derived from XRPD data acquired at 303 or 403 K. To verify the role of temperature in determining this discrepancy, thermal expansion coefficients were evaluated in the case of

Ni-bpz, ‡ the unit cell parameters of which vary linearly with temperature.¹⁹ Values of $-9.7 \cdot 10^{-5}$, $9.4 \cdot 10^{-5}$, $-2.2 \cdot 10^{-4}$ and $-2.2 \cdot 10^{-4} \text{ K}^{-1}$ were obtained for *a*, *b*, *c* and *V*, respectively. It is thus clear that temperature cannot be considered (at least alone) responsible for the discrepancies between experimental and calculated parameters. As a matter of fact, materials possessing the topology of our Ni(II) derivatives show a certain degree of flexibility if perturbed by external stimuli. A cornerstone example in this respect is represented by the MIL-53 family.¹⁷ As already pointed out by recent works^{35,49} on MIL-53(Al,Cr), breathing of the channels in these materials is the result of a fine equilibrium of strong and weak interatomic forces: in particular, dispersive interactions at long

‡ Unfortunately, as can be appreciated in Ref.¹¹, the unit cell parameters of Ni-bpb do not vary with a linear trend as a function of temperature: hence, estimating thermal expansion coefficients is not straightforward.

range can be of crucial importance.³⁵ This might be another reason for the expansion of the rhombic cavities observed in the predicted structures with respect to the experimental ones, even if the strong donor properties of the pyrazolate ligands render the structure less flexible than MIL-53.

The comparison of calculated bond distances with those retrieved from X-ray powder diffraction^{11,19} is not fully consistent because a rigid model has been used to describe the ligands in the latter case (see previous section).

3.2 Electronic Band Structure and Dielectric Properties

The electronic band structure and density of states (DOSs) of the two examined systems are displayed in Figure 3. For the two MOFs, a very similar band gap of 3.39 eV for Ni-bpz and 3.33 eV for Ni-bpb is predicted. The presence of the phenylene ring in Ni-bpb does not lead to modifications in the electronic band structure. Only a slight decrease of the band gap value due to the presence of the electronic levels of the aromatic rings at the top of the valence states is observed. The electronic bands of both systems are almost flat and featureless. The analysis of the highest occupied valence band and of the lowest unoccupied conduction band through projected DOSs, as reported in Figure 3, shows that in the former there is a predominant character due to the *p* orbitals of the pyrazolic carbon atoms and to the *d* orbitals of the Ni atoms, while in the latter the main contribution is given by the *d* orbitals of the Ni atoms with a small contribution of the *p* orbitals of the N atoms.

A semi-quantitative comparison between the calculated band gap values and the experimental evidence can be performed by looking at Figure 4, in which the Diffuse Reflectance (DR)UV-Visible spectra of Ni-bpz and Ni-bpb (solid lines, part a) and part b) respectively) and of their respective ligands (H₂bpz and H₂bpb, dashed lines) are reported. In both cases, the contribution of the ligands to the spectra of the corresponding MOF is quite clear. In particular, when compared with that of the H₂bpz ligand (featuring a broad band from 6 to 4.3 eV and then a shoulder from 4.3 to 3 eV), the optical spectrum of Ni-bpz (Figure 4a) reveals three new bands at 4.04, 3.43 and 2.64 eV. On the other hand, Ni-bpb exhibits minor differences with respect to the H₂bpb ligand, showing this one a broader absorption (from 6 to 3 eV and then a shoulder from 3 to 2 eV), probably because of the delocalization induced by the phenylene ring. The only distinguishable similar component in the spectra of the two MOFs is the band at 2.64 eV, which can be assigned to the fundamental band gap. The B3LYP hybrid functional has been demonstrated to be rather accurate in reproducing fundamental band gaps^{50,51}, even if it tends to overestimate the band gap of MOFs by about 16%³⁴. By taking this into account, for the investigated materials a value of ~ 2.8 eV can be estimated in reasonable agreement with the

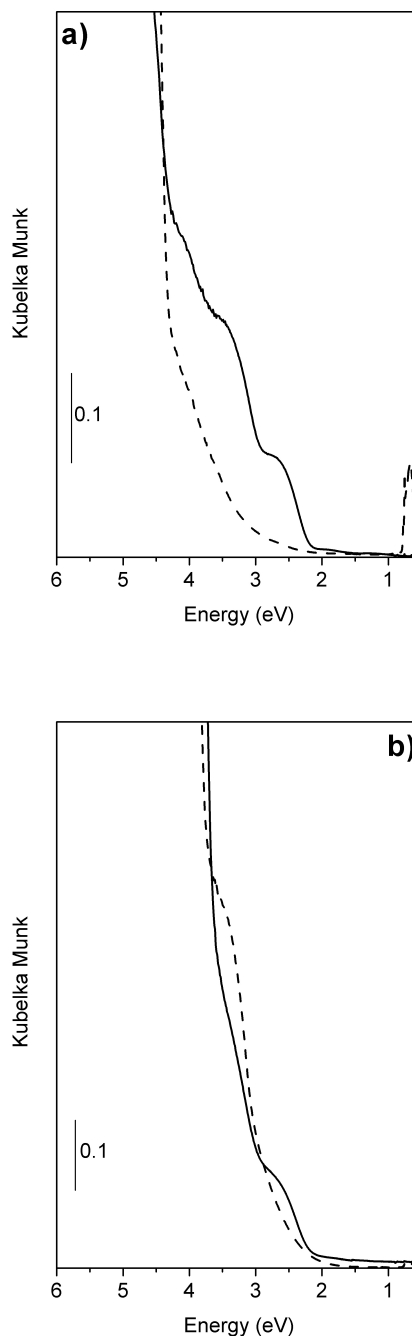


Fig. 4 DRUV-Visible-NIR spectra of Ni-bpz and H₂bpz (solid and dashed line respectively, part a) and Ni-bpb and H₂bpb (solid and dashed line respectively, part b)). In order to avoid saturation and to consider the relative intensity of the bands, the samples have been diluted with teflon.

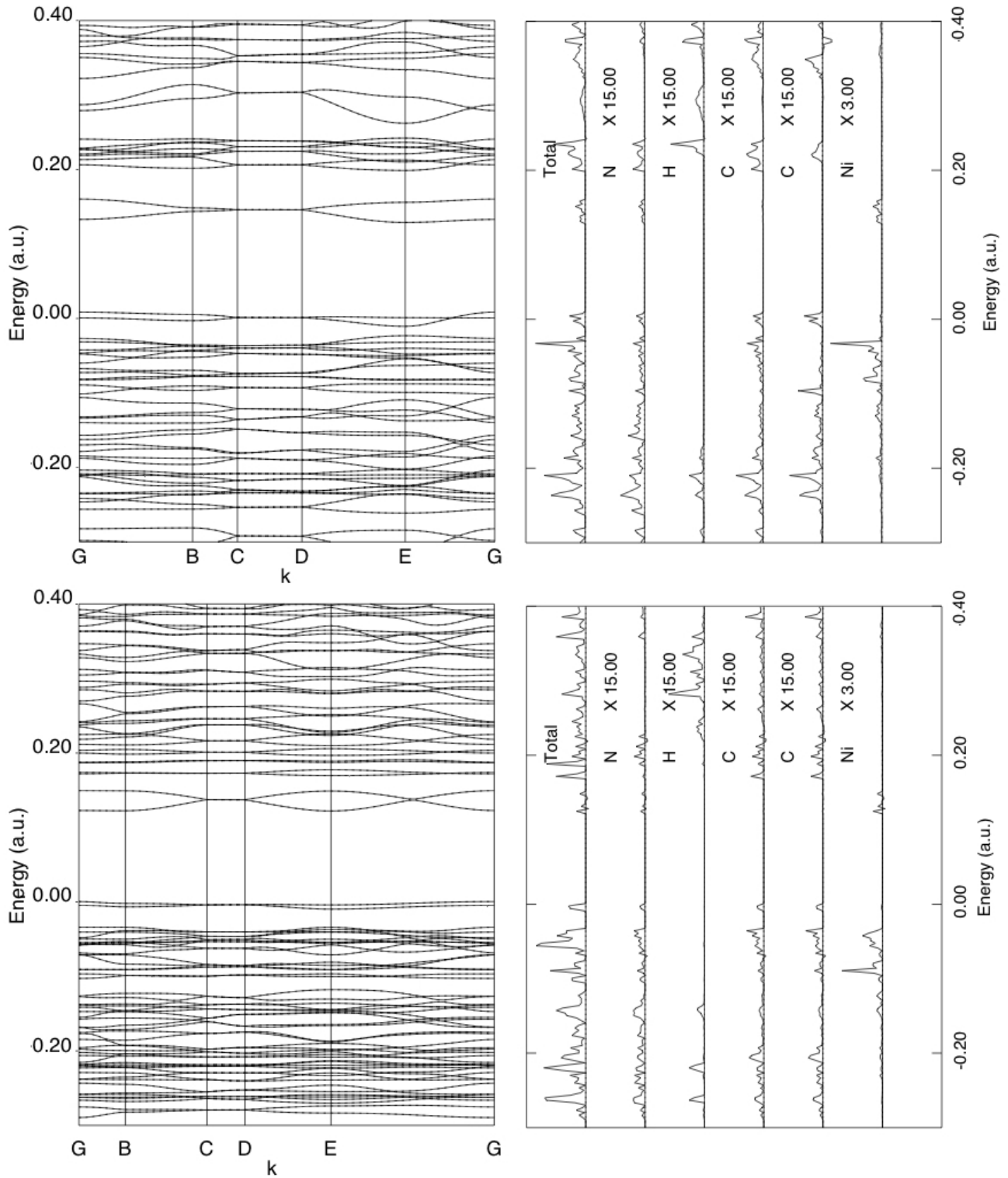


Fig. 3 Electronic band structure, total and projected density of states of Ni-bpz (top) and Ni-bpb (bottom). On the x -axis the points G, $A(\frac{1}{2}, 0, 0)$, $B(\frac{1}{4}, \frac{1}{4}, \frac{1}{4})$, $C(0, 0, \frac{1}{2})$, $D(-\frac{1}{2}, \frac{1}{2}, \frac{1}{2})$ and G correspond to \mathbf{k} points of the selected paths in the first Brillouin zone. Fermi level has been set at the zero of the energy.

experimental value. All the bands observed for both of them can be ascribed to Ligand to Metal Charge Transfer (LMCT) transitions from the respective ligands to Ni(II). This is also supported by the computed DOSs.

Since the MOFs under study have a band gap similar to common semiconductors (e.g. CdS=2.5 eV, ZnO=3.4 eV⁵²), it is interesting to extend the theoretical characterization to dielectric properties as well. Indeed, the presence of pores (voids) reduces the dielectric constant of the material and makes it interesting for application as low- k dielectric in electronic components⁵³. In Table 2 the computed unit cell polarizability, dielectric tensor and refractive index at the static limit of Ni-bpz and Ni-bpb are reported. According to the principal axes orientation, the metallic rows grow along the x direction, while y and z directions are referred to the major and minor diagonal of the rhombic channels (see Figure 1), respectively.

The polarizability tensor values are larger in the y and z directions, where the organic component lies. Inclusion of a phenylene ring as in the bpb ligand leads to an overall increase of all the components of the polarizability tensor, in particular along the y and z directions, as expected because of the larger degree of delocalization of the π -electrons. A small increase is also observed along the direction where the metallic rows grow.

In spite of the larger polarizability of Ni-bpb with respect to Ni-bpz, their dielectric tensor is quite similar: i.e. $1.88 < \epsilon_\infty < 2.38$ for Ni-bpz and $1.70 < \epsilon_\infty < 2.09$ for Ni-bpb. This is due to the inverse relationship between the dielectric constant and the unit cell volume (see eq. 2), with the latter being larger for Ni-bpb than Ni-bpz. A mean value ranging from 1.85 to 2.16 makes then these MOFs, as anticipated, interesting candidates as low- k materials in comparison with typical materials employed in electronics⁵⁴ such as silicon dioxide ($\epsilon = 4.3$), F-SiO₂ ($\epsilon = 3.8$) and hybrid organic-SiO₂ materials ($\epsilon = 2.8$).

3.3 Vibrational Frequencies: Calculated and Experimental FTIR Spectra

In this part we analyse the vibrational properties of the MOFs under investigation by comparing computed values and experimental data obtained from FTIR measurements.

The calculated frequencies of Ni-bpz and Ni-bpb are classified by symmetry, according to the $Imma$ and the $I112/b$ space group, respectively. The resulting irreducible representation of the normal modes at the Γ -point are as follows:

$$\text{Ni-bpz: } \Gamma^{90} = 11A_g(R) + 10B_{1g}(R) + 10B_{2g}(R) + 11B_{3g}(R) + 11A_u(In) + 13B_{1u}(IR) + 12B_{2u}(IR) + 12B_{3u}(IR)$$

$$\text{Ni-bpb: } \Gamma^{150} = 36A_g(R) + 36B_g(R) + 38A_u(IR) + 40B_u(IR)$$

For Ni-bpz, one of each B_{1u} , B_{2u} and B_{3u} modes corresponds to an acoustic mode (i.e. $\omega = 0$ at Γ) while for Ni-bpb such

modes are $2B_u$ and $1A_u$. Computed IR active modes are thus 32 and 75 for Ni-bpz and Ni-bpb, respectively (see Tables S1 and S3).

Figure 5 shows the calculated (black) and experimental (red) spectra of Ni-bpz and Ni-bpb (obtained after activation of the sample, see Figures S1 and S2) in the range between 1600 and 400 cm^{-1} . Note that the calculated frequencies above 600 cm^{-1} have been scaled by a factor 0.975 to achieve a better agreement with the experimental ones. This is a standard procedure in molecular calculations.⁵⁵⁻⁵⁷ For the sake of brevity, the spectral region between 3300 and 2900 cm^{-1} is reported, for both species, as supporting information (see Figure S5).

In spite of the high number of IR active modes predicted by the calculations, the observed bands with relevant intensities are roughly one half. This is because most of the computed IR modes are doublets with frequency values very close to each other.

As shown in Figure 5, the experimental and simulated spectra are in excellent agreement for both MOFs, especially in the unscaled low-frequencies region. Hence, this allows us to fully assign the experimental bands to the computed normal modes. Table 3 summarizes this assignment for the most relevant IR active bands in the range 1600-400 cm^{-1} . At higher wavenumbers (i.e., $\omega > 2900 \text{ cm}^{-1}$) the agreement is less satisfactory (see ESI), mainly as the result of the anharmonic character of the CH stretching modes that dominate that part of the spectrum.

When comparing the spectral region in which Ni-bpz and Ni-bpb share similar vibrational modes, it appears that the inclusion of the *para*-phenylene group in Ni-bpb slightly influences the frequency values because of couplings in the vibrational modes. In both materials those bands involving the atoms around the Ni(II) ions can be found between 500 and 400 cm^{-1} . Bands in the range 550-530 cm^{-1} are specific of Ni-bpb and can be assigned to in-plane and out-of-plane deformations of the phenylene rings. Instead, the bands in the region 700-650 cm^{-1} are characteristic of the pyrazolic group, with modes involving in-plane and out-of-plane deformations. Out-of-plane bendings of the pyrazolic -CH group are assigned to the bands at about 850-800 cm^{-1} . In Ni-bpb, these modes are coupled with out-of-plane deformations of the phenylene -CH. In the range 950-920 cm^{-1} , the observed bands can be associated to the in-plane bending of the C-C-C group of the pyrazolic ring. Comparing such mode in Ni-bpz and Ni-bpb, it can be observed that, in Ni-bpb, its coupling with in-plane deformations of the phenylene group increases its frequency from 917 to 953 cm^{-1} . The in-plane bending of the CH group belonging to the pyrazolic ring lies at about 1060 cm^{-1} both for Ni-bpz and Ni-bpb. Finally, the bands at higher frequencies (i.e. in the range 1100-1600 cm^{-1}) can be assigned to the symmetric and asymmetric stretching modes of the N-N, C-N and C-C bonds. Overall, inclusion of the *para*-phenylene

Table 2 Computed polarizability tensor (α), dielectric tensor (ϵ) and refractive index (n) values for Ni-bpz and Ni-bpb at the static limit (i.e. $\omega = 0$). α and ϵ in a.u.

	Ni-bpz			Ni-bpb			
	xx	yy	zz	xx	yy	xz	zz
α	342.5	385.8	246.7	467.6	672.8	26.1	428.3
ϵ_∞	2.226	2.381	1.883	1.759	2.093	0.042	1.696
n	1.492	1.543	1.372	1.324	1.448	0.239	1.302

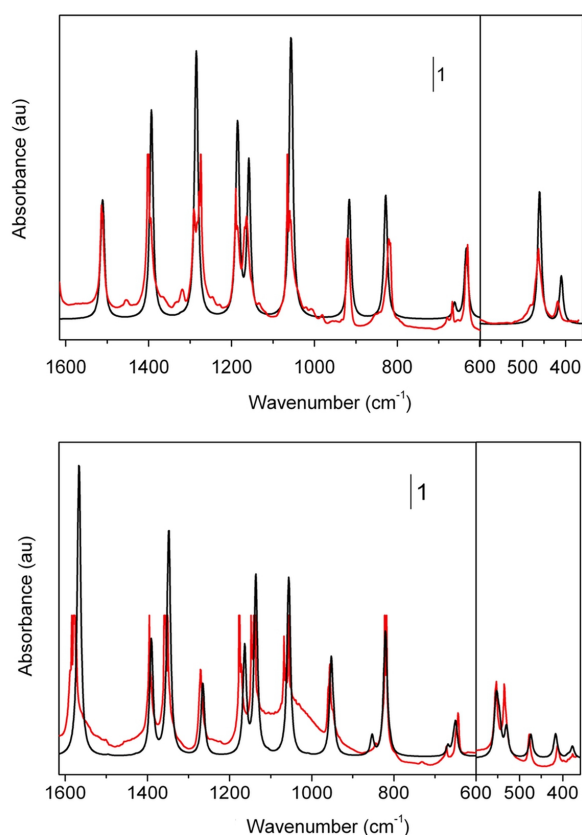


Fig. 5 Simulated (black) and experimental (red) FTIR spectra of Ni-bpz (top) and Ni-bpb (bottom). The calculated frequencies above 600 cm^{-1} are scaled by a factor of 0.975 to best fit the experimental IR spectra in the range $1600\text{-}400\text{ cm}^{-1}$. The simulated spectra have been computed by using a Lorentzian function with a FWHM of 15 cm^{-1} .

Table 3 Calculated and experimental IR frequencies (cm^{-1}) of Ni-bpz and Ni-bpb in the range $1600\text{-}600\text{ cm}^{-1}$ with the description of the normal modes.

Ni-bpz		Ni-bpb		Description ^b
Calc ^a	Exp	Calc ^a	Exp	
410	420	380	380	Asym stretch Ni-N
		414	412	Sym stretch Ni-N
461	465	472	479	Bend op N-Ni-N
		530	533	Deform ip ligand
		553	553	Deform op C-C(Φ)-C(Φ)
633	634			Bend sym op N-C-H
		649	643	Bend op C-C-C(Φ)
662	667	669	671	Deform op pyraz
827	820	820	821	Bend op H-C pyraz + H-C phenyl ring in-phase
916	918			Bend ip C-C-C
		952	957	Bend ip C-C-C + Bend op asym H-C-C
1058	1060	1055	1055	Bend ip sym H-C-C
1184	1191	1138	1139	Stretch N-N
1157	1164	1162	1176	Bend ip asym H-C-C
		1267	1270	Bend ip N-C-H
1284	1277	1347	1350	Stretch sym C-N
1393	1403	1390	1395	Stretch asym C-N
1510	1513	1566	1578	Stretch sym C-C-C pyrazolic

^aCalculated frequencies above 600 cm^{-1} are scaled by a factor of 0.975.

^b ip=in-plane, op=out-of-plane

ring in the bispyrazolate ligand leads to both an increase and a decrease of the vibrational frequencies.

3.4 H₂ Adsorption in Ni-bpb

The presence of coordinatively unsaturated Ni(II) ions is one of the most interesting features of the examined MOFs. There-

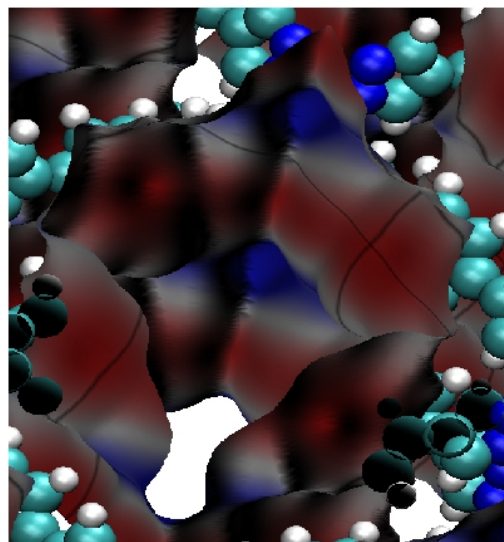
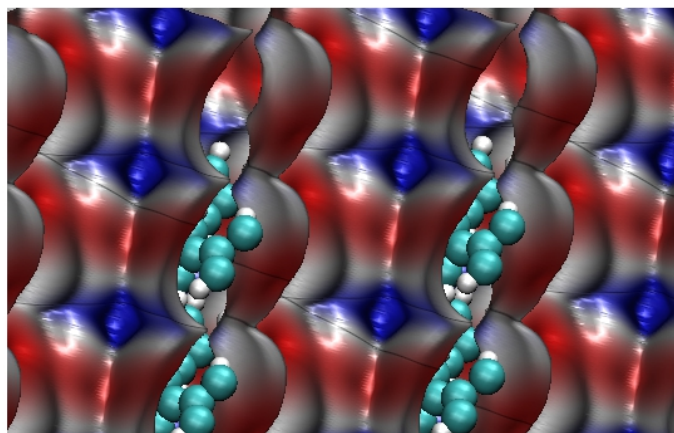


Fig. 7 Two different views of the electrostatic potential of Ni-bpb mapped on a charge density isosurface of 0.001 au. Negative regions are red, while neutral and positive areas are shown in white and blue, respectively.

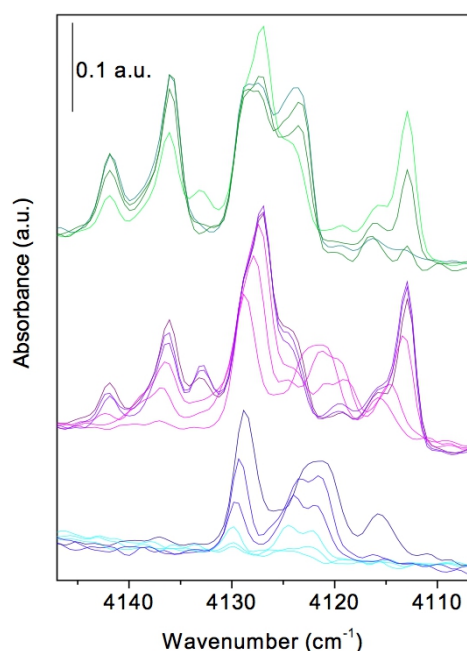


Fig. 6 FTIR spectra of the H₂ adsorption in Ni-bpb at different temperatures: 87-56 K (bottom), 56-14 K (middle) and 14 K (top).

fore, the adsorption capability of such materials was investigated through the use of different small probe molecules.

Among them, we will discuss in the following only the performance of Ni-bpb towards molecular hydrogen, because of its relevance for the so called hydrogen economy.⁵⁸

The stretching vibration mode of H₂ is IR inactive but it becomes active when the molecule interacts with a polarizing center able to perturb it by lowering its point group symmetry. In Raman spectroscopy (where the stretching mode ν is active), there are two signals at different frequencies for the two spin isomers (i.e. ortho and para) because of the anharmonicity. The two peaks lie at 4161 cm⁻¹ (para) and at 4155 cm⁻¹ (ortho). For the unperturbed H₂ molecule we consider the Raman stretching frequency at 4161 cm⁻¹ (parahydrogen). Interaction with a surface implies the appearance of IR bands which are usually red-shifted proportionally to the interaction strength. It has been observed, in the case of organic or inorganic microporous and mesoporous materials, that very weak H₂ adsorptions are associated with bands at frequencies ≤ 4120 cm⁻¹ ($|\Delta\nu| \geq 40$ cm⁻¹) (this spectral range includes also the features associated with liquid-like and physisorbed hydrogen). When the interaction occurs with polarizing centers (cations^{26,59,60}, anions, or anion/cation couples⁶¹), the vibrational spectroscopic evidence strongly depends on the interaction site (i.e. charge/radius value²⁶, presence of d orbitals⁵⁹ and first coordination sphere^{62,63}). In this case, the bands can be found in the range between 4120 and 3900 cm⁻¹.

In Figure 6, the FTIR spectra resulting from the interaction of H₂ molecules with a batch of Ni-bpb cooled in isobaric conditions are reported. The spectra have been divided into three groups to make the description easier. The bottom series

collects the spectra obtained in the range 87-56 K; the middle set contains the spectra between 56 and 14 K, and, finally, the upper group reports the contact time effect at 14 K.

At 83 K, the first bands appear at 4129, 4124 and 4122 cm^{-1} . This spectral region indicates very weak H_2 interactions and it excludes specific hydrogen-open metal interactions, although the Ni(II) atoms have two coordinative vacancies. All the bands grow simultaneously, which means that there are several adsorption sites with comparable stability.

In the 56-14 K range we can observe, in addition to the growth of the above bands, the appearance of new bands at higher frequencies (4142, 4136 and 4132 cm^{-1}) and a new complex absorption centered at 4112 cm^{-1} . This band is indicative of the presence of a limited number of sites, not easily accessible, and of a high perturbative activity toward hydrogen. The presence of these not easily accessible sites is confirmed by calculated 3D plots of the electron density with the electrostatic potential mapped on top (see Figure 7).

When the system reaches equilibrium at 14 K, the principal absorptions lie at 4141, 4136, 4127 and 4112 cm^{-1} .

For the interpretation of these observations, it is useful to recall what was previously observed for other MOFs. In the case of MOF-5, only a weak adsorption of H_2 on aromatic rings was observed with the corresponding IR bands located in the range between 4110 and 4140 cm^{-1} ¹⁸. On the contrary, in the case of activated CPO-27-Ni, in which Ni(II) is fivefold-coordinated, the Ni(II)- H_2 interaction is already visible at 110 K, as witnessed by several bands between 4020 and 4040 cm^{-1} not reversible at 14 K¹⁸. The relevant differences of this last case with the present results confirm the very weak interaction of the probe with the Ni(II) sites in Ni-bpb, and the prevalent adsorption on the organic linkers that leads to weak and non specific interactions.

Because of the negligible interactions between H_2 and the open metal sites of Ni-bpb, we did not attempt any calculation upon the adsorption of this probe molecule by the Ni(II) ions. Conversely, we tried to elucidate the reason for this non specific adsorption by investigating the electrostatic potential in the rhombic channels. Indeed, a very important surface property of a porous material is the electrostatic potential immediately over the surface, because it allows to better understand, at least qualitatively, the adsorption phenomena. In Figure 7, the electrostatic potential mapped on a charge density isosurface of 0.001 a.u. is displayed. From Figure 7, a negative region around the aromatic rings and a positive one at the Ni(II) sites can be appreciated. Interestingly, the positive cavities near the metallic ions, although clearly visible, appear to be partly shielded by the organic ligands and thence they are not easily accessible. In addition, the polarizing ability of Ni(II) appears to be lower than in other MOFs. For instance, Born atomic charges of Ni(II) in Ni-bpz and Ni-bpb are remarkably smaller than in CPO-27-Ni (i.e. ~ 1.25 vs 2.24) in which ad-

sorption of probe molecules, such as CO and CO_2 , has been predicted from ab-initio calculations³⁶ and verified by FTIR measurements¹⁶.

This could be one of the reasons why, although the Ni(II) ions of the title MOFs have coordinative vacancies, monitored by FTIR adsorption experiments with some probe molecules, such as H_2 , they do not show any specific interaction with the probe itself.

Most of the IR bands can therefore be attributed to the interaction between H_2 molecules and the organic part of the framework, especially with the phenylene group. When increasing the density of adsorbed molecules and decreasing the temperature, we believe that new equilibrium conditions are established. These involve a reorganization of H_2 molecules inside the cavities of the MOF giving rise to very complex spectra.

To explain the scarce affinity of Ni-bpb towards both H_2 and other probe molecules, such as CO and CO_2 [§], we hypothesize that a specific interaction with Ni(II) is strongly unfavored because of: (i) the cost in energy to change the spin state upon adsorption; (ii) steric effects as highlighted by the 3D maps of electron density/electrostatic potential; (iii) a low polarizing ability toward adsorbates and (iv) possible structural relaxation effects as a consequence of the increase of the coordination around Ni(II). In particular, the main obstacle to adsorption is likely to be the cost in energy due to the change in the coordination number of Ni(II) from 4 to 5, and to the change of the spin state from low-spin to high-spin. As discussed previously, the energy difference between the diamagnetic phase and the magnetic phases with Ni(II) in high-spin state is very large and amounts to +65 kJ/mol per Ni atom (see ESI for details). Therefore, for adsorption to take place, the interaction energy must be at least large enough to permit the change of the spin state of the transition metal ion; moreover, we expect a further cost to be paid because the change in coordination would also require a rearrangement of the structure around the adsorption site.

4 Summary and conclusions

In this work we have reported on the structural, electronic, dielectric and vibrational properties of two metal-organic frameworks that are built with Ni(II) ions, in square-planar coordination, linked through bipyrazolate ligands. Ab initio periodic B3LYP calculations, DRUV-Vis and FTIR experiments have been combined to fully characterize the examined materials. Overall, both materials show similar properties mainly due to the structural motif around the metal atoms. The main results can be summarized as follows: (i) both materials are diamagnetic, as expected for the square-planar coordination of Ni(II)

§ For CO and CO_2 , FTIR measurements did not provide any evidence of a specific interaction between the molecular probe and the open metal ion (see supporting information Figures S3 and S4)

and confirmed by theoretical results; (ii) they show a predicted band gap of about 3.0 eV, as confirmed by DRUV-Vis experiments, similar to wide-gap semiconductors with potentially interesting dielectric properties due to the microporous structure and the low dielectric constant; (iii) for Ni-bpb, FTIR measurements show that, at variance with other MOFs, the coordinatively unsaturated Ni(II) is not able to act as an open metal site for adsorption.

The latter is one of the most interesting result of this work. We have explained this unexpected behavior of Ni-bpb on the basis of the square-planar coordination of Ni(II) which greatly stabilizes a low spin state. Adsorption on Ni(II) would require an increase of coordination from 4 to 5 or 6 that corresponds to a change of Ni(II) spin state from low- to high-spin. The cost in energy to this change is predicted to be larger than expected interaction energies.

Present results show that MOFs with Ni(II) in a square-planar coordination are less effective for adsorption processes of simple molecules (i.e. H₂, CO₂,...) on the coordinatively unsaturated metal, while non-specific interactions seems to be responsible of the adsorption of larger molecules (e.g. cyclohexane and thiophene) as observed for Ni-bpb¹¹. Thence, the examined MOFs still remain interesting for size and shape selectivity adsorption processes.

In conclusion, we expect that the scarce adsorption capacity of exposed Ni(II) is a common feature of other MOFs with the same structural motif. Therefore, this is an important evidence to guide the synthesis of more selective Ni(II) based MOFs toward different kind of geometries for the open metal site.

Acknowledgment

Authors would like to thank Prof. Silvia Bordiga and Prof. Norberto Masciocchi for helpful discussions.

References

- 1 J. R. Long and O. M. Yaghi, *Chem. Soc. Rev.*, 2009, 1213–1215.
- 2 G. Férey, *Dalton Trans.*, 2009, 4400.
- 3 D. Farrusseng, S. Aguado and C. Pinel, *Angew. Chem. Int. Ed.*, 2009, **48**, 7502.
- 4 S. T. Meek, J. A. Greathouse and M. D. Allendorf, *Adv. Mater.*, 2011, **23**, 249–267.
- 5 N. R. Champness, *Dalton Trans.*, 2011, **40**, 10311.
- 6 K. S. Park, Z. Ni, A. P. Côté, J. Y. Choi, R. Huang, F. J. Uribe-Romo, H. K. Chae, M. O’Keeffe and O. M. Yaghi, *Proc. Nat. Acad. Sci. USA*, 2006, **103**, 10186.
- 7 H. J. Choi, M. Dincă and J. R. Long, *J. Am. Chem. Soc.*, 2008, **130**, 7848.
- 8 J.-P. Zhang and S. Kitagawa, *J. Am. Chem. Soc.*, 2008, **130**, 907.
- 9 H. J. Choi, M. Dincă, A. Dailly and J. R. Long, *Energy Environ. Sci.*, 2010, **3**, 117.
- 10 A. Maspero, S. Galli, N. Masciocchi and G. Palmisano, *Chem. Lett.*, 2008, **37**, 956–957.
- 11 S. Galli, N. Masciocchi, V. Colombo, A. Maspero, G. Palmisano, F. J. López-Garzón, M. Domingo-García, I. Fernández-Morales, E. Barea and J. A. R. Navarro, *Chem. Mater.*, 2010, **22**, 1664–1672.
- 12 N. Masciocchi, S. Galli, V. Colombo, A. Maspero, G. Palmisano, B. Seyyedi, C. Lamberti and S. Bordiga, *J. Am. Chem. Soc.*, 2010, **132**, 7902.
- 13 L. Valenzano, B. Civalleri, S. Chavan, S. Bordiga, M. H. Nilsen, S. Jakobsen, K. P. Lillerud and C. Lamberti, *Chem. Mater.*, 2011, **23**, 1700–1718.
- 14 S. Chavan, J. G. Vitillo, D. Gianoglio, O. Zavorotynska, B. Civalleri, S. Jakobsen, M. H. Nilsen, L. Valenzano, C. Lamberti, K. P. Lillerud and S. Bordiga, *Phys. Chem. Chem. Phys.*, 2012, **14**, 1614–1626.
- 15 L. Valenzano, B. Civalleri, S. Chavan, G. T. Palomino, C. O. Areán and S. Bordiga, *J. Phys. Chem. C*, 2010, **114**, 11185–11191.
- 16 L. Valenzano, J. G. Vitillo, S. Chavan, B. Civalleri, F. Bonino, S. Bordiga and C. Lamberti, *Catal. Today*, 2012, **182**, 67–79.
- 17 C. Serre, F. Millange, C. Thouvenot, M. Nogué, G. Marsolier, D. Louër and G. Férey, *J. Am. Chem. Soc.*, 2002, **124**, 13519–13526.
- 18 J. Vitillo, L. Regli, S. Chavan, G. Ricchiardi, G. Spoto, P. D. C. Dietzel, S. Bordiga and A. Zecchina, *J. Am. Chem. Soc.*, 2008, **130**, 8386–8396.
- 19 C. Pettinari, A. Tábačaru, I. Boldog, K. V. Domasevitch, S. Galli and N. Masciocchi, *Inorg. Chem.*, 2012, **51**, 5235–5245.
- 20 G. Spoto, E. N. Gribov, G. Ricchiardi, A. Damin, D. Scarano, S. Bordiga, C. Lamberti and A. Zecchina, *Prog. Surf. Sci.*, 2004, **76**, 71–146.
- 21 A. A. Tsyganenko, P. Y. Storozhev and C. O. Areán, *Kinet. Catal.*, 2004, **45**, 530–540.
- 22 G. Spoto, S. Bordiga, A. Zecchina, D. Cocina, E. N. Gribov, L. Regli, E. Groppo and C. Lamberti, *Catal. Today*, 2006, **113**, 65–80.
- 23 C. O. Areán, D. Nachtigallova, P. Nachtigall, E. Garrone and M. N. Delgado, *Phys. Chem. Chem. Phys.*, 2007, **9**, 1421–1436.
- 24 E. Garrone and C. O. Areán, *Chem. Soc. Rev.*, 2005, **34**, 846–857.
- 25 P. Nachtigall, O. Bludsky, L. Grajciar, D. Nachtigallova, M. N. Delgado and C. O. Areán, *Phys. Chem. Chem. Phys.*, 2009, **11**, 791–802.
- 26 C. O. Areán, G. T. Palomino, E. Garrone, D. Nachtigallova and P. Nachtigall, *J. Phys. Chem. B*, 2006, **110**, 395–402.
- 27 J. G. Vitillo, L. Regli, S. Chavan, G. Ricchiardi, G. Spoto, P. D. C. Dietzel, S. Bordiga and A. Zecchina, *J. Am. Chem. Soc.*, 2008, **130**, 8386–8396.
- 28 G. Spoto, J. G. Vitillo, D. Cocina, A. Damin, F. Bonino and A. Zecchina, *Phys. Chem. Chem. Phys.*, 2007, **9**, 4992–4999.
- 29 E. N. Gribov, D. Cocina, G. Spoto, S. Bordiga, G. Ricchiardi and A. Zecchina, *Phys. Chem. Chem. Phys.*, 2006, **8**, 1186–1196.
- 30 A. D. Becke, *J. Chem. Phys.*, 1993, **98**, 5648.
- 31 C. Lee, W. Yang and R. G. Parr, *Phys. Rev.*, 1998, **B37**, 785.
- 32 R. Dovesi, V. R. Saunders, C. Roetti, R. Orlando, C. M. Zicovich-Wilson, F. Pascale, B. Civalleri, K. Doll, N. M. Harrison, I. J. Bush, P. D’Arco and M. Llunell, *CRYSTAL09*, 2009, **University of Torino, Torino**, year.
- 33 R. Dovesi, R. Orlando, B. Civalleri, C. Roetti, V. R. Saunders and C. M. Zicovich-Wilson, *Z. Kristallogr.*, 2005, **220**, 571.
- 34 B. Civalleri, F. Napoli, Y. Noel, C. Roetti and R. Dovesi, *CrystEngComm*, 2006, **8**, 364–371.
- 35 A. M. Walker, B. Civalleri, B. Slater, C. Mellot-Draznieks, F. Corà, C. M. Zicovich-Wilson, G. Román-Pérez, J. M. Soler and J. D. Gale, *Angew. Chem. Int. Ed.*, 2010, **122**, 7663–7665.
- 36 L. Valenzano, B. Civalleri, K. Sillar and J. Sauer, *J. Phys. Chem. C*, 2011, **115**, 21777–21784.
- 37 F. Weigend and R. Ahlrichs, *Phys. Chem. Chem. Phys.*, 2005, **7**, 3297.
- 38 C. G. Broyden, *Math. Comput.*, 1965, **19**, 577–593.
- 39 D. D. Johnson, *Phys. Rev. B*, 1988, **38**, 12807–12813.
- 40 F. Pascale, C. M. Zicovich-Wilson, F. L. Gejo, B. Civalleri, R. Orlando and R. Dovesi, *J. Comput. Chem.*, 2004, **25**, 888.
- 41 C. M. Zicovich-Wilson, F. J. Torres, F. Pascale, L. Valenzano, R. Orlando, and R. Dovesi, *J. Comput. Chem.*, 2008, **29**, 2268.
- 42 M. Ferrero, M. Rerat, R. Orlando and R. Dovesi, *J. Comp. Chem.*, 2008, **29**, 1450.
- 43 M. Ferrero, M. Rerat, R. Orlando and R. Dovesi, *J. Chem. Phys.*, 2008, **128**, 014110.

-
- 44 M. Ferrero, M. Rerat, B. Kirtman and R. Dovesi, *J. Chem. Phys.*, 2008, **129**, 244110.
- 45 N. Masciocchi, F. Castelli, P. M. Forster, M. M. Tafoya and A. K. Cheetham, *Inorg. Chem.*, 2003, **42**, 6147–6152.
- 46 N. Masciocchi, G. A. Ardizzoia, S. Brenna, G. LaMonica, A. Maspero, S. Galli and A. Sironi, *Inorg. Chem.*, 2002, **41**, 6080–6090.
- 47 A. L. Spek, *J. Appl. Crystallogr.*, 2003, **36**, 7–13.
- 48 F. A. Cotton, G. Wilkinson, C. A. Murillo and M. Bochmann, *M. Bochmann*, Wiley-Interscience, NY, 1999, p. 1355.
- 49 D. S. Coombes, F. Corà, C. Mellot-Draznieks and R. G. Bell, *J. Phys. Chem. C*, 2009, **113**, 544–552.
- 50 J. Muscat, A. Wander and N. M. Harrison, *Chem. Phys. Lett.*, 2001, **342**, 397.
- 51 S. Tomić, B. Montanari and N. M. Harrison, *Physica E*, 2008, **40**, 2125.
- 52 B. G. Streetman and S. Banejee, *S. Banejee*, Prentice Hall, NJ, 2000, p. 524.
- 53 K. Zogorodniy, G. Seifert and H. Hermann, *Appl. Phys. Lett.*, 2010, **97**, 251905.
- 54 W. Volksen, R. D. Miller and G. Dubois, *Chem. Rev.*, 2010, **110**, 56–110.
- 55 A. P. Scott and L. Radom, *J. Phys. Chem.*, 1996, **100**, 16502.
- 56 M. P. Andersson and P. Uvdal, *J. Phys. Chem. A*, 2005, **109**, 2937.
- 57 J. P. Merrick, D. Moran and L. Radom, *J. Phys. Chem. A*, 2007, **111**, 11683–11700.
- 58 G. W. Crabtree, M. S. Dresselhaus and M. V. Buchanan, *Phys. Today*, 2004, **57**, 39.
- 59 G. Spoto, E. Gribov, S. Bordiga, C. Lamberti, G. Ricchiardi, D. Scarano and A. Zecchina, *Chem. Commun.*, 2004, 2768–2769.
- 60 J. G. Vitillo, A. Damin, A. Zecchina and G. Ricchiardi, *J. Chem. Phys.*, 2005, **122**, 114311.
- 61 F. J. Torres, J. G. Vitillo, B. Civalieri, G. Ricchiardi and A. Zecchina, *J. Phys. Chem. C*, 2007, **111**, 2505–2513.
- 62 A. Zecchina, S. Bordiga, J. G. Vitillo, G. Ricchiardi, C. Lamberti, G. Spoto, M. Björger and K. P. Lillerud, *J. Am. Chem. Soc.*, 2005, **127**, 6361–6166.
- 63 S. Bordiga, E. Garrone, C. Lamberti, A. Zecchina, C. O. Areán, V. B. Kazansky and L. M. Kustov, *J. Chem. Soc. Faraday Trans.*, 1994, **90**, 3367–3372.